# Flow and Transport in Unsaturated Fractured Rock: Effects of Multiscale Heterogeneity of Hydrogeologic Properties

Quanlin Zhou (QLZhou@lbl.gov) (correspondence author)

Hui-Hai Liu (HHLiu@lbl.gov)

Gudmundur S. Bodvarsson (GSBodvarsson@lbl.gov)

Curtis M. Oldenburg (CMOldenburg@lbl.gov)

Fax: 01-510-486-5686

Earth Sciences Division, Lawrence Berkeley National Laboratory, Berkeley, California

## Abstract

The heterogeneity of hydrogeologic properties at different scales may have different effects on flow and transport processes in a subsurface system. A model for the unsaturated zone of Yucca Mountain, Nevada, is developed to represent complex heterogeneity at two different scales: (1) layer scale corresponding to geologic layering and (2) local scale. The layer-scale hydrogeologic properties are obtained using inverse modeling, based on the available measurements collected from the Yucca Mountain site. Calibration results show a significant lateral and vertical variability in matrix and fracture properties. Hydrogeologic property distributions in a two-dimensional, vertical cross section of the site are generated by combining the average layer-scale matrix and fracture properties with local-scale perturbations generated using a stochastic simulation method. The unsaturated water flow and conservative (nonsorbing) tracer transport through the cross section are simulated for different sets of matrix and fracture property fields. Comparison of simulation results indicates that the local-scale heterogeneity of matrix and fracture properties has a considerable effect on unsaturated flow processes, leading to fast flow paths in fractures and the matrix. These paths shorten the travel time of a conservative tracer from the source (repository) horizon in the unsaturated zone to the water table for small fractions of total released tracer mass. As a result, the local-scale heterogeneity also has a noticeable effect on global tracer transport processes, characterized by an average breakthrough curve at the water table, especially at the early arrival time of tracer mass. However, the effect is not significant at the later time after 20% tracer mass reaches the water table. The simulation results also verify that matrix diffusion plays an important role in overall solute transport processes in the unsaturated zone at Yucca Mountain.

**Keyword:** Heterogeneity; Flow and transport; Fractures and matrix; Dual-permeability media; Unsaturated zone; Yucca Mountain

## 1. Introduction

The subsurface commonly exhibits multiscale heterogeneity in its hydrogeologic properties, with varying statistical characteristics, and thus different effects on flow and transport, depending on the process scale. Investigation of heterogeneity at different scales and its effects on flow and transport processes is an important step in site characterization.

Characterization of field-scale heterogeneity has been a major research issue in the subsurface hydrology community for many years. Typical examples include the Borden aquifer (Canada) and Cope Cod aquifer (Massachusetts, USA) where extensive measurements have been conducted for characterizing the spatial variability of hydrogeologic properties for multiphase flow (e.g., permeability and capillary pressure parameters) (e.g., Sudicky 1986; Kueper and Frind, 1991; Turke and Kueper, 1996; Hess et al., 1992). In the Borden aquifer, soils are fine-to-medium-grained beach sands with numerous lenses of coarse-to-silty fine-grained sand. The Cope Cod aquifer is composed of coarse-grained sand and gravel, grading to medium and fine sands. In both aquifers,

only the local-scale spatial variability was derived by filtering large-scale trends, because geologic layering is neither present nor needed in analyzing the effect of heterogeneity on field-scale flow and transport. Based on the estimated spatial variability of permeability and capillary parameters in the Borden aquifer, Kueper and Frind (1991) investigated the effect of local-scale heterogeneity on multiphase flow under different flow conditions. The transport of dense nonaqueous phase liquids (DNAPLs) and remediation in heterogeneous systems representing the Borden aquifer were also investigated by a number of researchers (e.g., Brown et al., 1994; Kueper and Gerhard, 1995; Mayer and Miller, 1996; Unger et al., 1998; Frind et al., 1999; Dekker and Abriola, 2000a,b). Jacobs (1999) derived the field-scale effective properties of multiphase flow in these two aquifers using spectral-perturbation analysis. Zhou et al. [2002] obtained significant effects of local-scale heterogeneity on two-phase flow in the Borden aquifer using numerical simulations. In characterizing such porous medium systems, a stationary mean process is usually assumed, and all parameters for the spatial variability of hydrogeologic properties are directly estimated from measured data, with no calibration involved.

Another example is the thick unsaturated zone (UZ) at Yucca Mountain, Nevada, the potential repository site for high-level nuclear waste. Compared with the aquifers discussed above, the UZ at Yucca Mountain is a more complex system consisting of alternating sequences of variably fractured and faulted welded and nonwelded tuffs, leading to two scales of heterogeneity: (1) layer-scale heterogeneity and (2) local-scale variations within each layer. Extensive scientific investigations have been conducted for the site characterization of Yucca Mountain, including surface mapping, the drilling of a large number of deep and shallow boreholes and tunnels, measurements and field tests, estimation of hydrogeologic properties, and flow and transport simulations (e.g., Bodvarsson et al., 1999). To characterize the subsurface heterogeneity and to understand its effects on flow and transport processes, the U.S. Geological Survey (USGS) has obtained substantial measurement data from the site (Rousseau, 1996; Flint, 1998a,b; Rousseau et al., 1997a,b). These data include measurements of state variables (e.g., water saturation and water potential) and core-scale rock properties (e.g., porosity, permeability, and capillary parameters for rock matrix). Additionally, pneumatic pressure, fracture mapping, and air-permeability data are also available for estimating fracture properties. These data were used for the analysis of effective hydrogeologic properties (Bandurraga and Bodvarsson, 1999; Liu et al., 2000; Ahlers and Liu, 2000) for the three-dimensional UZ flow model. However, only the average layer-scale (layer-averaged) rock properties were calibrated and used for the UZ flow model, neglecting local-scale heterogeneity and the lateral variability of layer-scale properties. Nevertheless, the existence of local-scale heterogeneity can be seen from the variations of measured state variables and properties within a layer. Flint (1998b) showed lateral variability of measured porosity within each layer. Bandurraga and Bodvarsson (1999) investigated the lateral variability of layer-scale matrix properties and showed that the lateral variability had an effect on radionuclide transport from the repository to the water table. Bodvarsson et al. (2001b) found considerable influence of local-scale heterogeneity of fracture permeability (only in a given geologic unit) on flow and transport by assuming different correlation lengths (1 and 3 m). However, the effect of multiscale heterogeneity (for both fracture and matrix properties) on unsaturated flow and radionuclide transport processes in the UZ of Yucca Mountain has not been fully investigated.

The objective of this paper is to investigate multiscale heterogeneity in the unsaturated fractured rock at Yucca Mountain and its effect on unsaturated flow and transport processes. In Section 2, we develop a conceptual model for representing heterogeneity at different scales in a layered subsurface reservoir, consisting of average layer-scale hydrogeologic properties and their corresponding local-scale perturbations. In Section 3, we analyze the measured state variables of ambient unsaturated flow and measured hydrogeologic properties and desaturation data, obtained mainly at the core scale. Correlation lengths for the local-scale properties are derived using core-scale permeability and porosity measurements. In Section 4, the spatial variability of some sensitive layer-scale hydrogeologic properties of matrix and fractures are calibrated (as well as the average layer-scale values for other properties) in the framework of forward simulation of unsaturated liquid flow (for matrix properties) and unsaturated liquid-gas flow (for fracture permeability). Finally, using numerical simulations, we investigated the effects of heterogeneity at different scales on unsaturated liquid flow (assuming a passive gas) and nonsorbing tracer transport.

# 2. Conceptual and Mathematical Model

## 2.1. Conceptual Model for Field Heterogeneity

In general, three different macroscopic scales can be used to define heterogeneity in the subsurface: (1) site (or field) scale; (2) layer scale; and (3) local scale. The site scale represents the entire solution domain used for modeling global flow and transport. The layer scale represents geologic layering in the vertical direction. Within a layer, relatively uniform properties are present in both vertical and lateral direction, in comparison with the larger variations between different layers that may vary significantly in thickness. The local scale represents the variation of properties within a hydrogeologic layer. An example is the core-scale of borehole samples for intrinsic permeability of the matrix. The mean ($\mu_{L(\mathbf{x})}$) and standard deviation ($\sigma_{L(\mathbf{x})}$) (dependent only on the geologic layer $L(\mathbf{x})$, where $\mathbf{x}$ is the coordinate vector of a point) of a layer-scale property can be obtained by inverse modeling. The mean, standard deviation and correlation lengths are considered to be sufficient to describe the variation of a considered property (e.g., matrix permeability). The local-scale perturbation of a property can be considered as a zero-mean random variable. Its standard deviation and correlation lengths can be estimated from local-scale measurements by filtering the layer-scale trends of properties. In general, the three-dimensional random field of a hydrogeologic property in the field scale can be generated by combining a number of two-dimensional (plane) random fields of layer-scale mean processes (each of which corresponds to a geologic layer) and a three-dimensional field of local-scale perturbations generated using stochastic simulation.

In this study, a simplified form of a random field representing multiscale heterogeneity in a layered reservoir is used, consisting of the averaged layer-scale mean process and perturbations in the form:

$$p(\mathbf{x}) \approx \mu_{L(\mathbf{x})} + p'\left(\sigma, \varepsilon(\mathbf{x})\right) , \qquad (1)$$

where $p(\mathbf{x})$ denotes the random field of a property at the site scale, $p'$ is the perturbation depending on the total standard deviation, $\sigma$, and the normalized perturbation, $\varepsilon$, of zero-mean and unity standard deviation. The total standard deviation, $\sigma$, results from a combination of the layer-scale spatial variability, $\sigma_{L(\mathbf{x})}$, and a local-scale perturbation (relative to the layer-scale properties). It is assumed that (1) a mean process within each geologic layer is stationary, and its mean and standard deviation depend only on the layer in which a point is located, and (2) the normalized perturbation $\varepsilon$ is stationary at the site scale, obeying the local-scale spatial correlations. These assumptions facilitate the generation of site-scale random fields of hydrogeologic properties using stochastic simulation. Only one random field of $\varepsilon$ needs to be generated for a hydrogeologic property, and then the spatial distribution of this property is obtained by Eq. (1). If geologic layering is absent, the mean process is stationary at the site scale, and the layer scale is not relevant.

## 2.2. Mathematical Model for Flow and Transport

Numerical simulations of unsaturated flow and transport in fractured rock are used for investigating effects of heterogeneity at different scales. For completeness, we list the governing equations for the simulated flow and transport processes in this section.

The unsaturated flow equation for phase $\beta$ ($= w$ for water or $= g$ for gas) in an isotropic medium, in the absence of sources or sinks, can be written as:

$$\frac{\partial \phi S_\beta}{\partial t} = \frac{\partial}{\partial x_i}\left( \frac{k k_{r\beta}}{\mu_\beta}\left( \frac{\partial P_\beta}{\partial x_i} + \rho_\beta g \frac{\partial z}{\partial x_i} \right) \right) + q_\beta \ , \quad i = x, y, z, \tag{2}$$

where $\phi$ is the porosity, $k$ is the intrinsic permeability, $k_r$ is the relative permeability, $S$ is the fluid saturation, $P$ is the fluid pressure, $\rho$ is the fluid density, $\mu$ is the viscosity, $g$ is the gravitational acceleration, $x_i$ is the Cartesian coordinate in the ith direction, $z$ is the elevation, $t$ is the time, and $q_\beta$ is the mass exchange rate (for the $\beta$ phase) between fractures and rock matrix per unit volume of rocks. The fluid's mass transfer term, $q_\beta$, depends on the transfer coefficient, $\Gamma_\beta$, and the difference in hydraulic head between fractures and matrix. Note that Eq. (2) is closed with the constraints of $p_g = p_w + p_c$, and $S_w + S_g = 1.0,$ where $p_c$ is the capillary pressure. The van Genuchten (1980) formulation for capillary pressure and relative permeability may be used for the unsaturated flow. In the following forward simulation, we have two different situations. In the first situation, we simulate unsaturated liquid flow only and assume a passive gas phase. In the second situation, we simulate unsaturated gas and liquid flow in the framework of calibration of fracture permeability, using pneumatic pressure data.

The advective-diffusive equation for conservative non-absorbing tracer transport in the unsaturated fracture (or matrix) continuum can be written:

$$\frac{\partial \phi S_\beta c}{\partial t} = \frac{\partial}{\partial x_i}\left( -qc + \phi D \frac{\partial c}{\partial x_i} \right) + q_{mf} \, , \tag{3}$$

where $q$ is the specific discharge, $D$ is the molecular diffusivity, $c$ is the tracer concentration, and $q_{mf}$ is the source/sink term representing the tracer mass transfer between fractures and rock matrix. Within rock matrix, molecular diffusion plays the dominant role in transport in comparison with advection and dispersion, because velocity is very small. Within fractures, velocity is relatively high, and both advection and hydrodynamic dispersion are important for mass transport. Along the interface between fractures and rock matrix, mass transfer stems from matrix diffusion, depending on the interface area, gradient of concentration, and the matrix diffusivity. Therefore, solute transport in fractures can be retarded by interaction between rock matrix and fractures.

## 2.3. Model for Preferential Flow

The term "preferential flow" is often used to describe non-uniform water flow characterized by widely different local-scale velocities. The consequence of preferential flow is that a portion of the flowing water can be concentrated to move along certain pathways at rates that are significantly faster than the rest of flowing water. As a result, contaminants carried by the flowing water can reach a given depth (or a downstream distance) in less time than predicted by calculations assuming a uniform wetting front (NRC, 2001). The preferential flow often occurs in both saturated and unsaturated fractured media (e.g., Tsang et al., 1991, Bodvarsson et al., 1999). Note that mechanisms for preferential flow are different for saturated and unsaturated flow systems. Preferential flow mainly results from subsurface heterogeneity for a saturated system, while it is due to a combination of both subsurface heterogeneity and nonlinearity of unsaturated flow.

Discrete fracture network models have been developed and applied to flow and transport in saturated fractured rocks in some potential European sites for nuclear waste repositories (e.g., Cacas et al., 1990; Dverstorp et al., 1992; Smith et al., 1997; Barten et al., 2000). When applied to the fractured unsaturated zone, the discrete fracture network models require the ability to simulate flow in the matrix as well as in the fractures. Each fracture in the model must be assigned a hydraulic conductivity curve and a retention curve (or two capillary pressure parameters). Because of the demanding data requirements and scale for the problem considered here, we employ a continuum approach in this study, rather than the discrete fracture network models (NRC, 2001).

A specific continuum approach, the dual-permeability method, is used here to handle flow and transport in the unsaturated zone at Yucca Mountain as well as the interaction of flow and transport between rock matrix and fractures (Warren and Root, 1963; Pruess and Narasimhan, 1985). The reason for using this method is that both matrix flow and fracture flow are involved, with dominant matrix flow within nonwelded geologic units and dominant fracture flow within welded units. Doughty (1999) investigated the feasibility of a variety of numerical approaches to treat fracture-matrix interactions at Yucca Mountain, including an effective continuum model (ECM), dual-porosity model, and dual-permeability model. Her conclusion is that the dual-permeability model seems to be adequate for unsaturated flow and transport of conservative (nonsorbing) tracers at the Yucca Mountain site.

The active fracture model is used to deal with preferential flow in unsaturated fractures at Yucca Mountain (Liu et al., 1998). This model is based mainly on the

hypothesis that only a portion of connected fractures are active in conducting water, as a result of preferential flow. This model has been used extensively for the site characterization of Yucca Mountain. Previous calibration at Yucca Mountain (Ahlers and Liu, 2000) indicates that only 20% of the connected fractures are active.

# 3. Measurements of Unsaturated Flow and Hydrogeologic Properties

## 3.1. Geologic Setting

A number of boreholes have been drilled for characterizing the ambient unsaturated zone at Yucca Mountain. Ten deep boreholes penetrate several stratigraphic units hundreds of meters (typically 600 m) in thickness. Many of them extend from the ground surface to the water table. Figure 1 shows locations of deep and shallow boreholes in the horizontal plane, as well as the underground Exploratory Studies Facility (ESF) and the Enhanced Characterization of Repository Block (ECRB) cross-drift tunnels. All deep boreholes are located far apart, whereas some shallow boreholes are located close to each other in the form of clusters.

Figure 2 shows the geologic layering within an east-west cross section through borehole UZ-14 at Yucca Mountain. Geologic formations have been grouped into stratigraphic units on the basis of welding (Montazer and Wilson, 1984). The stratigraphic units consist of the following, descending in order from the land surface: the welded Tiva Canyon Tuff (TCw), the mainly nonwelded Paintbrush Group (PTn), the welded Topopah Spring Tuff (TSw), the mostly nonwelded and sometimes altered Calico Hills Formation (CHn), and the mostly nonwelded and altered Crater Flat undifferentiated Group (CFu). The nonwelded zones near the water table in the CHn and CFu units may contain zeolitic alteration, reducing the matrix permeability by orders of magnitude (Bandurraga and Bodvarsson, 1999). Furthermore, 35 hydrogeologic layers are defined to correspond to geologic formations and coincident hydrogeologic unit boundaries.

The layer-scale spatial variability of hydrogeologic properties is investigated by calibrating these properties based on field observations. Most measurements of state variables and rock properties have been made at small scales and cannot be directly used in the site-scale flow model. Measured properties (such as matrix and fracture permeability and capillary parameters) will first be used for deriving their averaged values at the layer scale, which will be considered as prior information on layer-scale properties in model calibrations. It is believed that the calibration process implicitly involves upscaling from local-scale properties to appropriate ones at layer scale (Bodvarsson et al., 2001a).

## 3.2. Characterization of Unsaturated Flow

Ambient unsaturated flow at Yucca Mountain is controlled by both infiltration rate on the top boundary and the hydrogeologic properties of rocks. Near-surface infiltration data from Flint et al. (1996) suggest that significant infiltration occurs only every few years, in which the amount of infiltration still varies greatly because of storm amplitudes, durations, or frequencies. However, infiltration pulses are believed to be

retarded and attenuated by the PTn, leading to near steady-state conditions in the TSw unit (Bodvarsson et al., 1999). In this study, the spatially nonuniform average infiltration rate of about 5 mm/year at the mountain scale is assumed to be time-independent, and ambient steady-state unsaturated liquid flow is assumed. Measurements of three state variables of unsaturated flow (water saturation, water potential and pneumatic pressure) at the local scale have been obtained from a number of boreholes. The variations in these state variables are used to calibrate layer-scale hydrogeologic properties. To be consistent with the heterogeneity scale for calibration, the layer-scale value of a state variable in each hydrogeologic layer is obtained by averaging the local-scale data within this layer (Ahlers and Liu, 2000).

## Water Saturation

A large number of core-scale water saturation measurements were obtained at ten deep boreholes and some shallow ones (Rousseau et al., 1997a, b; Flint, 1998a). Figure 3 shows the vertical profiles of layer-scale matrix water saturation (in lines) at boreholes SD-12 and UZ-16. Water saturation in the welded TCw and TSw units is high, whereas it is relatively low at the nonwelded PTn unit, where the matrix intrinsic permeability is large. In the nonwelded CHn unit and below, water saturation distribution depends on the presence of zeolitic and vitric rocks. At borehole SD-12, the large variation in water saturation in the upper portion of CHn indicates the large variation in intrinsic permeability and capillary parameters between vitric layers of large permeability and underlying zeolitic layers of low permeability. At borehole UZ-16, no large variation in water saturation in the upper portion of CHn can be seen because no vitric layers are present. Finally, the devitrified layers in the CHn unit have much lower water saturation than the underlying and overlying layers. Figure 3 also shows the relatively small variations of core-scale water saturation (in dots) relevant to the layer-scale variations within each hydrogeologic layer. These variations result from local-scale variability in matrix permeability and capillary parameters.

Matrix water saturation is a signature of matrix-property heterogeneity under ambient quasi-steady-state flow, which is believed to prevail in the thick UZ at Yucca Mountain (Bodvarsson et al., 1999). Variations in water saturation may compensate for the effects of varying hydrogeologic properties. For example, in a low-permeability layer sandwiched into upper and lower layers of higher permeability, water saturation may be higher than in the neighboring layers, producing a higher relative permeability. This feature results in a small variation in actual permeability (a combination of relative permeability and the intrinsic permeability of the liquid phase). In addition, such a high water saturation in a low-permeability layer results in a small variation in water potential, compensating for the high variation caused by the high variability of characteristic capillary pressure under uniform saturation.

## Water Potential

Both *in-situ* and core water potential measurements are available for the rock matrix at some deep boreholes. Because of drying in the core-handling process, core water potential increases significantly, even when the reduction in water saturation is small (Rousseau et al., 1997a, b). For example, most core data suggest that the absolute

value of water potential at Yucca Mountain is in the range of 3-6 bars (Bodvarsson et al., 1999), while the *in-situ* water potential is in the range of 0.3-2.0 bars. Therefore, only the *in-situ* water potential data are used in the inverse modeling of hydrogeologic properties for the UZ flow. *In-situ* water potential data are available at five boreholes, each of which has less than ten data points available. As a result, few *in-situ* water potential data do play a less important role in inverse modeling than water saturation. Figure 4 shows the vertical profiles of measured *in-situ* water potential at borehole SD-12. Such *in-situ* data can be used directly in the calibration because these data are already at the layer scale.

#### Pneumatic Pressure

Pneumatic pressure measurements are useful in estimating fracture permeability, the key parameter in the welded geologic units (where fracture flow is dominant). Pneumatic pressure is indicative of naturally occurring subsurface gas flow caused by surface barometric pressure changes. Five boreholes are instrumented with isolated pressure transducers or pressure monitoring ports (Rousseau, 1996). The pneumatic records at all boreholes show common characteristics (Ahlers et al., 1999). Sensors in the TCw record little to no amplitude attenuation or phase lag with respect to the surface barometric signal. Sensors in the PTn unit record increasing attenuation and lag with depth below the top of the PTn. In most boreholes, sensors in the TSw unit record the same amount of attenuation and lag over the entire vertical interval of the TSw. Horizontally within the TSw, the observed attenuation and lag vary and appear to be governed by the thickness of the overlying PTn. Figure 11 shows the pneumatic pressure processes measured at four different sensors at borehole NRG-7a. It can be seen that significant attenuation occurs within the PTn unit, where matrix flow predominates.

## 3.3. Spatial Variability of Local-Scale Hydrogeologic Properties

Measurement of hydrogeologic properties has been conducted at different boreholes for porosity, intrinsic permeability, and capillary parameters. Data for the matrix rocks are representative of local-scale properties at the core scale. Core size is generally about 0.07 m in diameter. Measurements of intrinsic permeability and capillary parameters are used to derive layer-scale prior information for the calibration model. Correlation lengths at the local scale are estimated from the available permeability and porosity data for the matrix.

### 3.3.1. Data Available

#### Matrix Permeability

Measurements of core-sample intrinsic matrix permeability have been obtained from seven deep boreholes, not all of which are available in every present hydrogeologic layer. Figure 5 shows the vertical profile of measured intrinsic permeability (in dots) at borehole UZ-16. Matrix permeability is relatively small in the TCw unit and the entire TSw unit, but it is large in the thin PTn unit. In the zeolitic layers, permeability is small with small variability, while it is relatively high in the devitrified layers. Significant variations exist between different stratigraphic units. In addition, matrix permeability is too small to be measured (referred to as non-detected data) in a number of cores. The log

truncated permeability ($m^2$) for non-detected data is assumed to be –19.67, which is the smallest value in all of the detected measured permeabilities.

Figure 5 also shows the geometric mean (solid line) of measured permeability within each hydrogeologic layer at borehole UZ-16. When only detected data are available, the mean and standard deviation of log permeability is calculated using the available permeability measurements. When both non-detected and detected data are available in a layer, the geometric mean is obtained based on the assumption of lognormal distribution of permeability; the non-detected data points are ranked at the lowest permeability end of the distribution shown in Figure 6; the mean and standard deviation of log permeability is derived from the values of the detected permeability and their cumulative probability calculated based on the ranking. The geometric mean of permeability calculated may be smaller than the truncated value (shown in Figure 5), depending on the detected and non-detected data. For example, in a layer at borehole UZ-16, the available 23 non-detected data points and 11 detected points of very low permeability result in the (extrapolated) mean of log permeability of –20.14 ($m^2$). Figure 6 shows the estimation of mean and standard deviation of log permeability in the second case. It can be seen that the measured permeability obeys the assumed lognormal distribution (Ahlers and Liu, 2000).

For each layer at a deep borehole, the geometric mean and standard deviation of the measured log permeability are calculated. These two moments are specific to the considered layer and borehole in the individual inverse modeling analysis for estimating the lateral variability of intrinsic permeability. In addition, for each layer, the mean and standard deviation (layer-averaged) of local-scale log permeability are calculated by putting together all data in this layer from all the different boreholes to form a set of samples. These layer-averaged mean and standard deviations will be used in simultaneous inverse modeling for the first-order layer-scale mean process. When no data are available in a layer at a borehole, the layer-averaged moments are used for individual inverse modeling.

**Matrix Capillary Parameters**

The desaturation curve data (Flint, 1998a) show that there is no distinct entry capillary pressure, and therefore the van Genuchten (1980) characterization, which has been used extensively for the site characterization of Yucca Mountain, is employed here. Capillary parameters ($\alpha$ and $m$ for the van Genuchten (1980) characterization) are estimated from the desaturation data. These parameters are used to define the dependence of capillary pressure and relative permeability upon water saturation. Desaturation experiments have been conducted on 75 core samples obtained from deep boreholes (Flint 1998a). In each hydrogeologic layer, there is at least one set of data for the water saturation and capillary pressure curves. Maximum sets of seven are available for a layer in the TCw unit. The geometric mean of the estimated $\alpha$ and the standard mean of estimated $m$ are calculated for each layer. Because few data are available in many layers, a constant standard deviation of 0.65 is used for all layers and will be used in the following calibration (Ahlers and Liu, 2000).

**Fracture Permeability**

Fracture permeability in all hydrogeologic layers is calculated based on air permeability inferred from air-injection tests conducted in boreholes and ESF alcoves (LeCain, 1997; Rousseau et al., 1997a, b; Liu et al., 2000). The geometric mean and range of local-scale air permeability depend on the layer considered and the source of data (boreholes or niches). For example, the log local-scale permeability, measured in borehole NRG-6 in layer tsw34, varies from –12.8 to –10.5 ($m^2$), with a mean of –12.2, whereas the log air permeability measured at Niche 2 in the same layer varies from -14.8 to -9.9 (Liu et al., 2000, Figure 2). The mean fracture aperture for this layer is $9.8\times10^{-5}$ m. The geometric mean of the fracture permeability is assumed to reflect the upscaling from local scale to layer scale, with the resulting fracture permeability in each layer used as prior information in the following model calibration.

## 3.3.2. Correlation Lengths

At Yucca Mountain, core-property measurements were not designed to obtain accurate spatial correlation lengths because the spacing of measurements is not uniform in the vertical direction. In the horizontal direction, only some shallow boreholes with porosity measurements are located within a correlation length, and all deep boreholes with permeability measurements are located farther apart than a correlation length. Therefore, correlation lengths of matrix permeability at the local scale are roughly estimated from available core-scale measurements. In this study, it is assumed that the exponential covariance model is suitable (Gelhar, 1994). The correlation length is obtained using a non-linear curve fitting of data points.

Correlation length in the vertical direction is estimated from permeability data in deep boreholes. The sample spacing of some 2-5 m within some layers at a borehole does not vary significantly, making it possible to calculate the correlation lengths for such layers. Such quality permeability data are available only for several layers at borehole UZ-16 and two other deep boreholes. For each of these layers, we estimate the vertical correlation length using the permeability data with quasi-uniform spacing. The estimated vertical correlation length ($\lambda_z$) in different layers varies from 5 to 20 m, with an average of 10 m. Figure 7 shows the estimated vertical correlation length in four different layers at borehole UZ-16.

The horizontal correlation length is estimated from porosity measurements available in layers within several clusters of shallow boreholes, shown in Figure 1. For example, boreholes UZN53 through UZN55 are less than 100 m apart (Flint, 1998b). For two close boreholes, the covariance function, normalized by standard deviations, is estimated for a layer with a number of data points ($\geq 10$) in both boreholes. The average covariance function is then calculated for all available layers, leading to a data point in fitting the horizontal correlation length. Figure 8 shows the average horizontal correlation length ($\lambda_{xy}$) of approximately 120 m, estimated from porosity data in shallow boreholes. It is assumed that this horizontal correlation length can be used to approximate that of permeability at the local scale, because the correlation between porosity and permeability obtained from their measurement is good, except in zeolitic layers (Flint, 1998b).

# 4. Spatial Variability of Layer-Scale Hydrogeologic Properties

Layer-scale rock properties are calibrated using layer-scale state variables and prior information obtained in the previous section. The seven different rock properties to be calibrated include matrix permeability ($k_m$), matrix $\alpha_m$ and $m_m$ for the van Genuchten characterization, fracture permeability ($k_f$), fracture $\alpha_f$ and $m_f$, and the active fracture factor ($\lambda_f$) (Liu et al., 1998). The value of each property in each of the 35 hydrogeologic layers is estimated, leading to some 245 unknowns in the calibration model. Two steps are involved in the calibration process to reduce the uncertainty in the calibrated rock properties. In the first step, only the first-order moment (average value) of rock properties is calibrated by simultaneously using all measurements at different boreholes, producing vertical variability of rock properties uniform in the lateral direction. This calibration process is referred to as *simultaneous inverse modeling* (SIM). In the second step, the lateral variability of the three most sensitive properties ($k_m, k_f$, and $\alpha_m$) is further calibrated, with the others fixed at their calibrated values in the first step. For each deep borehole with measurements of state variables and/or prior information, the three sets of properties are calibrated for hydrogeologic layers present and with sufficient data. For each layer, the lateral variability of hydrogeologic properties is reflected through the variation of the calibrated values at different boreholes. This calibration process is referred to as *individual inverse modeling* (IIM).

In each of the two steps, calibration of matrix and fracture properties is done iteratively. First, matrix properties are calibrated using water saturation and potential data through steady-state unsaturated liquid flow simulation. Second, fracture properties are calibrated using pneumatic pressure data through transient simulation of the unsaturated gas and liquid flow, with all matrix properties fixed at their calibrated values in the current iteration. The iterative process continues until convergence is obtained.

For a deep borehole with available measurements of state variables and/or properties, a vertical column from the ground surface to the water table is extracted from a three-dimensional flow model. It is assumed that unsaturated flow in the column is vertical. This assumption is appropriate at Yucca Mountain except in layers below perched water in zeolitic layers (Wu et al., 1999). Different infiltration rates (mapped from the regional infiltration map) into the columns at different boreholes are used to maintain the ambient unsaturated flow conditions. Steady-state unsaturated liquid flow simulations are used to match field observations, and transient flow simulations are used to match pneumatic data. The ITOUGH2 code (Finsterle, 1999) is used for estimating the layer-scale hydrogeologic properties. This code was developed for general inverse modeling of reservoir simulation.

## 4.1. Simultaneous Inverse Modeling

In this calibration step, a uniform distribution of rock properties is assumed for each hydrogeologic layer. The layer-scale measured rock properties are averaged over all different boreholes, with the averaged values employed as prior information. The objective function is the sum of the mismatch of measured and simulated state variables

at each deep borehole and the mismatch of prior and calibrated properties averaged over all boreholes. The mismatches are weighted, based on standard deviation of the measured state variables and prior information. Calibrated results are shown in Table 13 in Ahlers and Liu (2000).

## 4.2. Lateral Variability of Rock Properties

Individual inverse modeling is conducted to evaluate the lateral variability of layer-scale rock properties. For each borehole, we calibrate the rock properties specific to the location of the borehole. For each layer, the calibrated value of a property at a borehole can be treated as a sample of this property in this layer. Samples at different deep boreholes are assumed to be independent because all of the boreholes are located far apart, and the number of samples depends on the number of boreholes used in the calibration process and the presence of this layer. The mean and standard deviation of the layer-scale rock properties is estimated from calibrated results at all participating boreholes. Matrix and fracture properties are calibrated in an iterative way (Bodvarsson et al., 2001a).

### Matrix Properties

Matrix properties are calibrated under steady-state flow conditions. Prior information includes measured intrinsic permeability and capillary parameter $\alpha_m$ values obtained through fitting desaturation curve data. The same prior information for matrix $\alpha_m$ is used for all boreholes, because desaturation data are available at only three boreholes. The SIM calibrated values of $\alpha_m$ are used as initial guesses. When permeability measurements are available within a layer at a borehole, their geometric mean is used as prior information; otherwise, the SIM calibrated value is used. Data from nine deep boreholes are available for calibrating these matrix properties. There is no measured state variable or prior information for all layers in any of the nine boreholes; at some boreholes, one or more layers are absent. As a result, the number of samples (calibrated properties) varies with different layers. The objective function consists of a mismatch between measured and simulated water saturation and water potential, and a mismatch between the prior and resulting properties.

Figure 9 shows matches between measured water saturation and simulated values at the final calibrated properties for borehole SD-12, as well as the mismatch of $k_m$ and $\alpha_m$ between their prior and calibrated values. The match of simulated and measured water saturation profile is good. Note that in simultaneous inverse modeling, the matrix and fracture properties at ch1v through ch5v layers are assumed to be identical. In the current individual inverse modeling, properties in these layers are allowed to vary. The same treatment is applied for layers ch2z through ch5z.

Figure 10 shows the spatial variability of $k_m$ and $\alpha_m$ in different hydrogeologic layers. The solid line represents the vertical profile of mean value for these properties, while the dashed line represents the range of standard deviation. Scatter points represent calibrated values at different boreholes obtained by individual inverse modeling. The lateral variability of $k_m$ is 2-3 orders of magnitude, smaller than the dominant vertical

variability of permeability in different stratigraphic units. For example, the variation of the mean permeability between the TSw and PTn units is 5-6 orders of magnitude, while mean permeability within each of the two units varies by 2-3 orders of magnitude. The matrix $\alpha_m$ varies laterally less than $k_m$, with the lateral variability of one order of magnitude. The vertical profile of the mean $\alpha_m$ is very similar to that obtained by simultaneous inverse modeling.

**Fracture Properties**

Fracture (intrinsic) permeability is calibrated using the pneumatic pressure data (Rousseau, 1996), after the matrix properties have been determined. These data are available at four deep boreholes, each of which contains just four sensors at different elevations. The pneumatic pressure measured at a sensor reflects the cumulative effects on the attenuation and phase shift (lag) of fracture permeability in all layers above the sensor. To improve the reliability of the calibrated $k_f$, a factor (ratio of calibrated value to the prior information) common for the entire PTn or TSw is used as an unknown, while the permeability in each present TCw layer is calibrated, following Ahlers and Liu (2000). Fracture $k_f$ in each layer below the TSw unit is fixed at its SIM calibrated value, which is close to the geometric mean of local-scale air permeability. Therefore, for each deep borehole, we have 5-6 unknowns ($k_f$) to be estimated.

Figure 11 shows a good match between the measured and calibrated pneumatic pressure values at four sensors in borehole NRG-7a. It can be seen that the greatest pneumatic pressure attenuation occurs in the PTn, where matrix flow is dominant and $k_f$ is smaller than in the overlying and underlying units. Little or no attenuation occurs in the TSw unit. Figure 12 shows the spatial variability of layer-scale $k_f$ in the TCw, PTn, and TSw units. The mean $k_f$ varies by more than one order of magnitude between the PTn and the underlying TSw unit. Within a unit, the small variation of layer-scale $k_f$ in the vertical direction is determined a-priori based on the geometric mean of local-scale air permeability and SIM results (LeCain, 1997); the layer-scale $k_f$ varies in the lateral direction by an order of magnitude. Note that the variation in the calibrated layer-scale fracture intrinsic permeability is much smaller than that in the local-scale fracture permeability inferred from air permeability measured at deep boreholes and ESF alcoves, as discussed above.

## 5. Effect of Multiscale Heterogeneity on Flow and Transport

A two-dimensional vertical cross section in the east-west direction through borehole UZ-14 is employed to investigate the effect of multiscale heterogeneity in matrix and fracture properties on unsaturated flow and conservative non-sorbing tracer transport at Yucca Mountain. The flow domain is bounded by the ground surface at the top and by the water table surface at the bottom. The average thickness of the domain is about 700 m, ranging in elevation from 730 m to 1,500 m, with length in the east-west

direction of about 4070 m. The repository is located in the TSw35 layer (an elevation of about 1,050 m).

We generate a non-uniform computational mesh for flow and transport simulation. A horizontal block is about 20 m in length and 30 m in width, with both smaller than the horizontal correlation length (120 m). Note that the width is arbitrary and only because TOUGH2 uses three-dimensional blocks, although the problem considered is two-dimensional. When a fault is present, a fault block is located at the exact fault horizontal coordinates, and the lengths of all blocks around the fault block are adjusted. In the vertical direction, a maximum thickness of 5 m for a column is used below the potential repository, and 2 m for the PTn unit. A minimum thickness of 0.2 m is set for the whole cross section. When a hydrogeologic layer at a horizontal column is thinner than the specified minimum thickness, this layer is absent in the property field, and its thickness is combined into a vertical block within its neighboring layers. As a result, the number of model layers within a horizontal column varies, depending on the thickness of hydrogeologic layers. There are 204 horizontal blocks in the lateral direction, including 4 fault blocks, whereas there are about 160 blocks in the vertical direction. In total, we have 34,000 3-D blocks for the matrix and 34,000 blocks for fractures using the dual-permeability method.

To investigate the effect of multiscale heterogeneity of rock properties on the unsaturated flow and transport, we generate and use the random fields of three selected properties (matrix permeability $k_m$, matrix $\alpha_m$, and fracture permeability $k_f$). For comparison, we employ different sets of rock property distributions in three cases. In Case A, no local-scale heterogeneity and lateral layer-scale variability of all properties is considered; this case corresponds with the conceptual model extensively used for Yucca Mountain. In Case B, local-scale heterogeneity and lateral layer-scale variability of $k_f$ only is considered. Local-scale perturbation and lateral layer-scale variability of both matrix and fracture (the three selected) properties are considered in Case C.

## 5.1. Random Fields of $k_m$, $\alpha_m$, and $k_f$

For this investigation, a 2-D heterogeneous system of rock properties in a uniform mesh is generated, based on the layer-scale variability of the three properties obtained in Section 4 and local-scale variability obtained in Section 3. This system consists of 2-D random fields of $k_m$, $\alpha_m$, and $k_f$. It is assumed that the three properties are mutually independent. The reason for this assumption is that the correlation between local-scale $k_m$ and $\alpha_m$ in different hydrogeologic layers is very different, with the correlation coefficient varying from 0.005 to 0.963, determined from just a few data points. Then we map the rock property fields into the non-uniform computational mesh.

For each of the three properties, a two-dimensional random field is generated on the basis of Eq. (1) with its layer-scale and local-scale statistical properties. The property domain is 4,600 m long and 1,000 m thick, with $230 \times 500$ blocks of $20\,m \times 2\,m$. The normalized perturbation in the entire cross section is generated using the sequential indicator stochastic simulation code in the GSLib, a geostatistic software library (Deutsch and Journel, 1998). The average vertical correlation length of 10 m and horizontal length

of 120 m are used with the exponential covariance model. It is assumed that the three properties obey lognormal distribution and are mutually independent. To avoid unreasonable geologic features in the random fields generated, we use an upper and lower bound of variation around the mean value of log-transformed variable for the three selected properties. For example, $k_f$ lies within the range of $\pm$ one order of magnitude around its geometric mean.

Figure 13 shows the generated log-value fields of $k_m$, $\alpha_m$, and $k_f$. The dominant layering of properties can be seen in each of the fields, as well as the local-scale random perturbations. Matrix permeability $k_m$ is relatively higher in the PTn unit than in the TSw and TCw units. This means that the local-scale variability of $k_m$ does not inundate the dominant contrast of $k_m$ between different stratigraphic units.

## 5.2. Effect on Unsaturated Flow

The steady-state unsaturated liquid flow conditions are simulated for different sets of property fields (Cases A, B, and C) using the TOUGH2 code (Pruess et al., 1999), a general-purpose reservoir simulator for multi-dimensional coupled fluid and heat flow of multiphase, multi-component fluid mixtures in porous and fractured media. On the top boundary, the non-uniform net-infiltration rate mapped from the infiltration rate map (Flint et al., 1996) at Yucca Mountain is specified. Because of the non-uniformity of infiltration, the average rate along the cross section (1.9 mm/year) differs from the average rate over the 3-D site-scale model (4.9 mm/year) (Wu et al., 1999). The bottom boundary corresponds to the water table. Both vertical side boundaries are assumed to be impervious to liquid flow. Note that the time-independent infiltration rate is used in this study. We will not investigate the effect of time-dependent infiltration (or pulse-event) or the reduction of the fracture-matrix coupling term on flow and transport, but the reader is referred to McLaren et al. (2000) for further details.

Figure 14 shows the difference in water saturation in fractures among Cases A, B, and C. The differences in fracture saturation between Cases B and C is smaller than that between Cases A and B. The reason is that Cases B and C share the same average layer-scale and local-scale variations of fracture permeability, while only averaged layer-scale fracture permeability is considered in Case A. The small difference in fracture saturation between Cases B and C stems from local-scale heterogeneity of matrix $k_m$ and $\alpha_m$. Therefore, as expected, the local-scale heterogeneity of fracture permeability plays a more significant role in affecting fracture saturation than the local-scale heterogeneity of matrix properties. Figure 15 shows the difference in fracture flux among Cases A, B, and C. Fracture flux deviates more significantly in Case C from that in Case A than Case B. This indicates the significant effect of local-scale matrix heterogeneity on fracture flux. In particular, matrix heterogeneity in the PTn unit (where matrix flow is dominant) redistributes the infiltration flux specified on the top boundary (ground surface), leading to a different flux field at the interface between the PTn and the underlying TSw units. Below this interface, matrix heterogeneity has little effect on fracture flux, because fracture flow is dominant within the TSw and CHn (zeolitic) unit.

Figure 16 shows simulated liquid flux in matrix and fractures at the repository horizon. The matrix flux in Case C varies significantly, as a result of matrix heterogeneity. The difference in matrix flux between Cases A and B is very small. This indicates that heterogeneity in fracture permeability alone has little effect on matrix flux, while matrix heterogeneity has a significant effect on matrix flux distribution. In comparison with the simulation results in Case A, Case C liquid flux increases in some vertical fractures (while it decreases in some other fractures) under the effect of matrix and fracture heterogeneity. At some locations, fast flow paths develop. The large difference (at the easting of 170,260 m) in repository-horizon fracture flux between Cases A and C reflects the total effect of matrix and fracture heterogeneity in the area above the repository horizon, especially above the PTn-TSw interface. The heterogeneity in fracture permeability alone has little effect on fracture flux at the repository horizon in the unsaturated zone of Yucca Mountain.

## 5.3. Effect on Tracer Transport

We also investigate the effect of multiscale rock heterogeneity on transport by simulating the transport of a conservative non-sorbing tracer for the different sets of property fields. Bodvarsson et al. (2001a) indicated, using sensitivity study, that fracture dispersivity has an insignificant effect on transport in the unsaturated zone at Yucca Mountain, in comparison with matrix diffusivity. In this study, a constant molecular diffusivity of $3.2\times10^{-11} m^2/s$ and dispersivity of zero are used in our simulations.

The T2R3D code is used for simulating tracer transport in the steady-state flow fields obtained above (Wu and Pruess, 2000). An initial concentration of 1.0 is specified in the repository-horizon fracture blocks and a concentration of 0.0 is specified in all other fracture and matrix blocks. The top model boundary and the vertical side boundaries are impervious to tracer transport because the tracer plume is far away from these boundaries. The bottom boundary is free-flow with zero diffusive flux (vertical gradient of concentration is zero). The tracer moves with the dominant downward liquid flow and flows out through the bottom boundary into the underlying saturated zone.

Figure 17 shows the fractional breakthrough curves of the cumulative mass at the water table. The fraction is defined as the ratio of the cumulative mass flowing out of the solution domain through the water table, to the total tracer mass initially released at the repository horizon. The tracer reaches the water table earlier in Case C than in Case A. For example, 1% tracer of fraction reaches the water table in about 5 years for Case C and 18 years for Case A. This results from fast flow paths for advective transport in some fractures, with higher flux in Case C than in Case A, as shown in Figure 16. With increasing time, the effect of fast flow paths decreases and the effect of slow paths increases. The combination of both effects can be seen from the curve slope, representing the mass reaching the water table in a unit time interval. Before 100 years, the slope in Case C is generally larger than that in Case A; after 100 years, mass from slow paths in Case C is dominant. The 20% fraction of the tracer reaches the water table at 512 years and 232 years in Cases A and C, respectively. Figure 17 also shows that the tracer reaches the water table slightly later for Case B, under the local-scale heterogeneity of fracture permeability alone, than for Case A.

Both saturation and flux distributions obtained in flow simulation may have an effect on tracer transport, as shown in the tracer transport equation, Eq. (3). To check the significance of the two distributions on transport, we add a new artificial case (Case D) by combining the liquid saturation field in Case A with the fluid flux in Case C. Then we run the decoupled transport simulation for Case D. Breakthrough curves for Cases C and D are almost identical. This indicates that the resulting flux distribution contributes to the deviation of the Case C breakthrough curve from the Case A one, whereas the saturation distribution has an insignificant effect on this deviation.

We also checked the significance of local-scale heterogeneity of flow properties and the uncertainty of molecular diffusivity in affecting tracer transport. A new case (Case E) for transport develops by reducing the molecular diffusivity from $3.2\times10^{-11}$ to $3.2\times10^{-12} m^2/s$, with all other hydrogeologic properties and flow conditions the same as in Case A. Then we run the transport simulation for Case E. As shown in Figure 17, the breakthrough curve is very sensitive to the molecular diffusivity used, indicating that matrix diffusion plays an important role in overall solute transport behavior in the UZ of Yucca Mountain. This finding can be interpreted using the transport equation (3) with the coupling terms between fractures and the matrix. The decreased matrix diffusivity results in less total tracer mass moving from fractures into the matrix. Tracer mass released into fractures at the repository horizon migrates downward to the water table with less matrix retardation. Therefore, tracer reaches the water table earlier than in Case A. For a higher fraction of tracer mass at the water table (say, 40%), the arrival time is also much earlier than in Case A. This also results from less mass storage in the matrix, with most mass remaining in fractures. At an even higher fraction (say, 83%), the difference in the arrival time between Cases E and A decreases, and finally, the arrival time in Case E is longer. The reason is that in early time, tracer mass enters the matrix from fractures with more difficulty in Case E because of the smaller diffusivity. At later time, tracer in the matrix migrates back to fractures with more difficulty in Case E, once little tracer mass remains in fractures. Therefore, it takes a much longer time for all mass to leave the solution domain in Case E than all the other cases. This finding is consistent with the findings of Bodvarsson et al. (2001a), who showed that matrix diffusion is an important mechanism for retarding radionuclide transport in unsaturated fractured rock. This finding is also consistent with that found for saturated flow, that the diffusivity of the rock matrix strongly influences transport behaviors (e.g., Hadermann and Heer, 1996; Barten et al., 2000).

## 6. Summary and Conclusions

A model has been developed to investigate the effects of multiscale heterogeneity on flow and transport in unsaturated fractured rock. In this model, the layer-scale mean properties and local-scale perturbations are combined to represent a heterogeneous, layered subsurface reservoir. This model has been applied to the unsaturated fractured zone at Yucca Mountain, Nevada. The layer-scale spatial variability of hydrogeologic properties was determined using inverse modeling, based on field measurements of state variables and rock properties. Significant variability was observed in both vertical and lateral direction, with the lateral variability within each layer smaller than the dominant vertical variability in larger-scale stratigraphic units.

A mountain-scale heterogeneous system, with random fields for three most sensitive properties, was generated, using the calibrated layer-scale properties and local-scale perturbations created by the sequential indicator stochastic simulation method. This generated heterogeneous system was compared with the one currently used for the site characterization of Yucca Mountain, which considers only the averaged mean processes of all rock properties. We simulated the unsaturated flow and transport of a conservative non-sorbing tracer in these systems using different scale heterogeneity. The flow simulation results show that the local-scale heterogeneity of matrix and fractures has an effect on unsaturated flow, resulting in fast flow paths in fractures and high flux variation in the matrix. Local-scale fracture heterogeneity alone has little effect on global flow regime, because flow in fractures is dominantly vertical. Local-scale matrix heterogeneity redistributes the matrix flux and leads to different flux into fractures along the interface between dominant matrix (above the interface) and fracture (below the interface) flow regimes. The transport simulation results show that the effect of local-scale matrix and fracture heterogeneity on global tracer transport (the breakthrough curve of a fraction of cumulative mass arriving at the water table from the repository) is considerable for the early time of tracer mass arriving at the water table. However, the effect is insignificant for the later time after 20% total mass reaches the water table. More importantly, the uncertainty in matrix diffusivity may produce more significant uncertainty in the breakthrough curve than the local-scale matrix and fracture heterogeneity at all simulation times, because matrix diffusivity directly affects the mass exchange between fractures and the rock matrix.

## Acknowledgments

The authors wish to thank B. H. Kueper at Queen's University, Canada and W. Barten at Paul Scherrer Institute (PSI), Switzerland for their careful review of the manuscript. We also wish to show our appreciation to Guomin Li of Berkeley Lab for his manuscript review. Thanks are also due to C.F. Ahlers, S. Finsterle, and L. Pan of Berkeley Lab for their help in this work. This work was in part supported by the Director, Office of Civilian Radioactive Waste Management, U.S. Department of Energy, through Memorandum Purchase Order EA9013MC5X between Bechtel SAIC Company, LLC, and the Ernest Orlando Lawrence Berkeley National Laboratory (Berkeley Lab).

## References

Ahlers, C.F., Liu, H.H., 2000. Calibrated properties model. Report MDL-NBS-HS-000003, Lawrence Berkeley National Laboratory, Berkeley, CA; CRWMS M&O, Las Vegas, NV.

Ahlers, C.F., Finsterle, S., Bodvarsson, G.S., 1999. Characterization and prediction of subsurface pneumatic response at Yucca Mountain, Nevada. J. Contam. Hydrol., 38 (1-3), 47-68.

Bandurraga, T.M., Bodvarsson, G.S., 1999. Calibrating hydrogeologic parameters for the 3-D site-scale unsaturated zone model of Yucca Mountain, Nevada. J. Contam. Hydrol., 38 (1-3), 25-46.

Barten W., Niemeyer, M.J., Jakob, A., 2000. Efficient junction sequence method for transport in a directed network. Water Resources Research, 36(5), 1333-1337.

Bodvarsson, G.S., Boyle, W., Patterson, R., Williams, D., 1999. Overview of scientific investigations at Yucca Mountain, Nevada, the potential repository for high-level nuclear waste. J. Contam. Hydrol., 38(1-3), 3-24.

Bodvarsson, G.S., Liu, H.H., Ahlers, R., Wu, Y.S., Sonnenthal, E., 2001a. Parameterization and upscaling in modeling flow and transport at Yucca Mountain. In Conceptual Models of Flow and Transport in the Fractured Vadose Zone, National Research Council. National Academy Press, Washington D.C.

Bodvarsson, G.S, Wu, Y.S., Zhang, K., 2001b. Development of discrete flow paths in unsaturated fractures at Yucca Mountain. J. Contam. Hydrol., to appear.

Brown, C.L., Pope, G.A., Abriola, L.M., Sepehrnoori, K., 1994. Simulations of surfactant-enhanced aquifer remediation. Water Resources Research, 30(11), 2959-2977.

Cacas, M.C., Ledoux, E., deMarsily, G., Barbreau, A., Calmels, P., Gaillard, B., Margritta, R., 1990. Modeling fracture flow with a stochastic discrete fracture network: Calibration and validation, 2, The transport model. Water Resources Research, 26, 491-500.

Dekker, T.J., Abriola, L.M., 2000a. The influence of field-scale heterogeneity on the infiltration and entrapment of dense nonaqueous phase liquids in saturated formations. J. Contam. Hydrol., 42, 187-218.

Dekker, T.J., Abriola, L.M., 2000b. The influence of field-scale heterogeneity on the surfactant-enhanced remediation of entrapped nonaqueous phase liquids. J. Contam. Hydrol., 42, 219-251.

Deutsch, C.V., Journel, V.G., 1998. GSLIB geostatistic software library and user's guide. Oxford University Press, New York.

Doughty, C., 1999. Investigation of conceptual and numerical approaches for evaluating moisture, gas, chemical, and heat transport in fractured unsaturated rock. J. Contam. Hydrol., 38, 69-106.

Dverstorp, B., Andersson, J., Nordqvist, W., 1992. Discrete fracture network interpretation of field tracer migration in sparsely fractured rock. Water Resources Research, 28(9), 2327-2343.

Finsterle, S., 1999. ITOUGH2 user's guide. Report LBNL-40040, UC-400, Lawrence Berkeley National Laboratory, Berkeley, CA.

Flint, A.L., Hevesi, J.A., Flint, L.E., 1996. Conceptual and numerical model of infiltration for the Yucca Mountain area, Nevada. U.S. Department of Energy Milestone Report 3GUI623M, 210 p, Las Vegas, NV.

Flint, L.E., 1998a. Matrix properties of hydrogeologic units at Yucca Mountain, Nevada. U.S.Geological Survey Open-File Report, MOL.19970324.0046, U.S. Geological Survey, Denver, CO.

Flint, L.E., 1998b. Characterization of hydrogeologic units using matrix properties, Yucca Mountain, Nevada. USGS Water resources investigation report 97-4243, Denver, CO.

Frind, E.O., Molson, J.W., Schirmer, M., Guiguer, N., 1999. Dissolution and mass transfer of multiple organics under field conditions: The Borden emplaced source. Water Resources Research, 35(3), 683-694.

Gelhar, L.W., 1994. Stochastic subsurface hydrology. Prentice Hall, Englewood Cliffs, NJ.

Hadermann, J., Heer W., 1996. The Grimsel (Switzerland) migration experiment: integrating field experiments, laboratory investigations and modeling. J. Contam. Hydrol., 21, 87-100.

Hess, K.M., Wolf, S.H., Celia, M.A., 1992. Large-scale natural gradient tracer test in sand and gravel, Cape Cod, Massachusetts: 3. Hydraulic conductivity variability and calculated macrodispersivities. Water Resources Research, 28(8), 2011-2027.

Jacobs, B.L., 1999. Effective properties of multiphase flow in heterogeneous porous media. Ph.D. Thesis, Massachusetts Institute of Technology.

Kueper, B.H., Frind, E.O., 1991. Two-phase flow in heterogeneous porous media: 2. model application. Water Resources Research., 27(6), 1059-1070.

Kueper, B.H., Gerhard, J.I., 1995. Variability of point source infiltration rates for two-phase flow in heterogeneous porous media. Water Resources Research, 31(12), 2971-2980.

LeCain, G.D., 1997. Air-injection testing in vertical boreholes in welded and nonwelded tuff, Yucca Mountain, Nevada. U.S. Geological Survey Water Resources Investigation Report 96-4262, GS960908312232.012 (Non-Q), GS960908312232.013 (Q), U.S. Geological Survey, Denver, CO.

Liu, H.H., Ahlers, C.F., Cushey, M.A., 2000. Analysis of hydrologic properties. Report ANL-NBS-HS-000002, Lawrence Berkeley National Laboratory, Berkeley, CA; CRWMS M&O, Las Vegas, NV.

Liu, H.H., Doughty, C., Bodvarsson, G.S., 1998. An active fracture model for unsaturated flow and transport in fractured rocks. Water Resources Research, 34(10), 2633–2646.

Mayer, A.S., Miller, C.T., 1996. The influence of mass transfer characteristics and porous media heterogeneity on nonaqueous phase dissolution. Water Resources Research, 32(6), 1551-1567.

McLaren, R.G., Forsyth, P.A., Sudicky, E.A., VanderKwaak, J.E., Schwartz, F.W., Kessler, J.H., 2000. Flow and transport in fractured tuff at Yucca Mountain: numerical experiments on fast preferential flow mechanisms. J. Contam. Hydrol., 43, 211-238.

Montazer, P., Wilson, W.E., 1984. Conceptual hydrologic model of flow in the unsaturated zone, Yucca Mountain, Nevada. USGS Water-Resources Investigations Report 84-4345, U.S. Geologic Survey, Lakewood, CO.

National Research Council, 2001. Conceptual models of flow and transport in the fractured vadose zone. National Academy Press, Washington D.C.

Pruess, K., Narasimhan, T.N., 1985. A practical method for modeling fluid and heat flow in fractured porous media, Soc. Pet. Eng. J., 25, 14-26.

Pruess, K., Oldenburg, C., Moridis, G., 1999. TOUGH2 user's guide. Report LBNL-43134, Lawrence Berkeley National Laboratory, Berkeley, CA.

Rousseau, J.P., 1996. Data transmittal of pneumatic pressure records from October 24, 1994 through July 14, 1996 for boreholes UE-25 UZ#14, UE-25 UZ#5, USW NRG-6, USW NRG-7a, USW SD-12 and USW UZ-7a, Yucca Mountain, Nevada. U.S. Geologic Survey, Denver, CO.

Rousseau, J.P., Loskot, C.L., Thamir, F., Lu, N., 1997a. Results of borehole monitoring in the unsaturated zone within the main drift area of the exploratory studies facility, Yucca Mountain, Nevada. USGS Milestone Report SPH22M3, U.S. Geologic Survey, Denver, CO.

Rousseau, J.P., Kwicklis, E.M., Grillies D.C., eds., 1997b. Hydrogeology of the unsaturated zone, north ramp area of the exploratory studies facility, Yucca Mountain, Nevada. USGS Water Resources Investigation Report 98-4045, U.S. Geologic Survey, Denver, CO.

Smith, P.A., Gautschi, A., Vomvoris, S., Zuidema, P., Mazurek, M., 1997. The development of a safety assessment model of the geosphere for a repository sited in the crystalline basement of northern Switzerland. J. Contam. Hydrol., 26, 309-324.

Sudicky, E.A., 1986. A natural gradient experiment on solute transport in a sand aquifer: spatial variability of hydraulic conductivity and its role in the dispersion process. Water Resources Research, 22(13), 2069-2082.

Tsang, C.F., Tsang, Y.W., Hale, F.V., 1991. Tracer transport in fractures: analysis of field data based on a variable aperture channel model. Water Resources Research, 27(12), 3095-3106.

Turke, M.A., Kueper, B.H., 1996. Geostatistical analysis of the Borden aquifer hydraulic conductivity field. J. Hydrology, 178(1-4), 223-240.

Unger, A.J., Forsyth, P.A., Sudicky, E.A., 1998. Influence of alternative dissolution models and subsurface heterogeneity on DNAPL disappearance times, J. Contam. Hydrol., 30, 217-242.

van Genuchten, M.T., 1980. A closed form equation for predicting the hydraulic conductivity of unsaturated soils. Soil Sci. Soc. Am. J., 44, 892-898.

Warren, J.E., Root, P.J., 1963. The behavior of naturally fractured reservoirs. Soc. Pet. Eng. J., 245-255, Transactions, AIME, 228.

Wu, Y.S., Ritcey, A.C., Bodvarsson, G.S., 1999. A modeling study of perched water phenomena in the unsaturated zone at Yucca Mountain. J. Contam. Hydrol., 38, 157-184.

Wu, Y.S., Pruess, K., 2000. Numerical simulation of non-isothermal multiphase tracer transport in heterogeneous fractured porous media. Advance in Water Resources, 23, 699-723.

Zhou, Q., Gelhar, L.W., Jacobs, B., 2002. Comparison of field-scale effective properties of two-phase flow in heterogeneous porous media obtained by stochastic analysis and numerical experiments. In Findikakis A.N. (Ed.), Proceedings of the international groundwater symposium on bridging the gap between measurements and modeling in heterogeneous media, Berkeley, California.

Figure 1. Location of all data points (for calibration model) of deep and shallow boreholes and underground tunnels (ESF and ECRB).

Figure 2. Hydrogeologic layers and faults in the two-dimensional vertical cross section through borehole UZ-14.

Figure 3. Vertical profiles of measured core-scale matrix water saturation (in dots) and their layer-scale values (in lines) at (a) borhole SD-12, and (b) borehole UZ-16. Observations provided by the USGS (Rousseau et al., 1997a, b; Flint, 1998a).

Figure 4. Vertical profile of in-situ water potential measurements at borehole SD-12. Observations provided by the USGS (Rousseau et al., 1997a).

Figure 5. Vertical profile of measured core-scale matrix permeability (in dots) and the layer-scale geometric mean (in line) at the UZ-16 borehole. Observations provided by the USGS (Flint, 1998a).

Figure 6. Estimation of the mean (the horizontal value at the scaled probability = 5) and standard deviation (the horizontal interval between two neighboring vertical ticks) of local-scale measured matrix permeability in a hydrogeologic layer at borehole UZ-16. Observations provided by the USGS (Flint, 1998a).

Figure 7. Estimation of vertical correlation lengths with the exponential covariance model in different layers using matrix permeability ($k$) at borehole UZ-16.

Figure 8. Estimation of average horizontal correlation length using porosity ($\phi$) measurements.

Figure 9. Match at borehole SD-12: (a) the measured water saturation profile and simulated one at the calibrated properties, (b) the prior information and the calibrated values of matrix permeability ($k_m$), and (c) the prior information and calibrated values of matrix $\alpha_m$.

Figure 10. Spatial variability of layer-scale matrix permeability $k_m\,(m^2)$ and $\alpha_m$ (pa) obtained by individual inverse modeling using borehole measurements.

Figure 11. Match between the measured pneumatic pressure processes (in lines), and simulated ones (in line-dots) at the calibrated properties at borehole NRG-7a at four sensors at different layers and elevations. Observations from October 1994 through July 1996 provided by the USGS (Rousseau, 1996).

Figure 12. Spatial variability of layer-scale fracture permeability ($m^2$) obtained by individual inverse modeling using borehole measurements.

Figure 13. The random fields of matrix permeability, matrix $\alpha$, and fracture permeability in the two-dimensional vertical cross-section through borehole UZ-14 generated using multi-scale heterogeneity.

Figure 14. Comparison of simulated fracture saturation at all nodes in Cases A, B and C.

Figure 15. Comparison of simulated fracture flux (m/s) at all nodes in Cases A, B and C.

Figure 16. Comparison of simulated matrix and fracture flux (m/s) at the repository horizon in Cases A, B, and C.

Figure 17. Comparison of breakthrough curve of the fraction of cumulative tracer mass arriving at the water table in Cases A, B, C, and E.

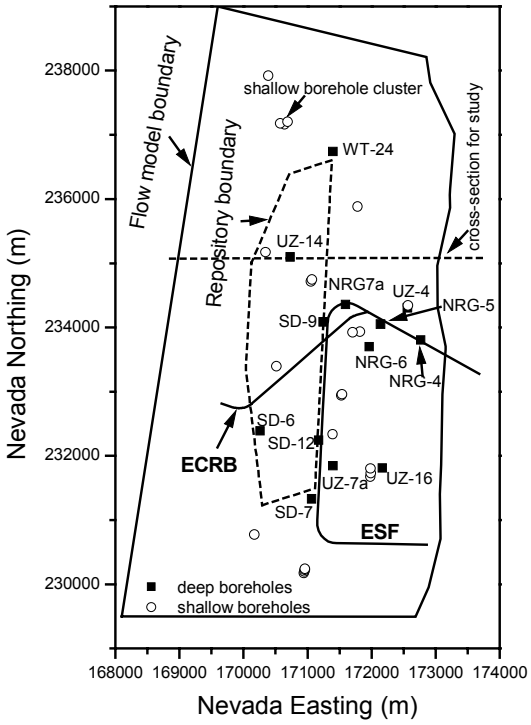


Figure 1. Location of all data points (for calibration model) of deep and shallow boreholes and underground tunnels (ESF and ECRB).

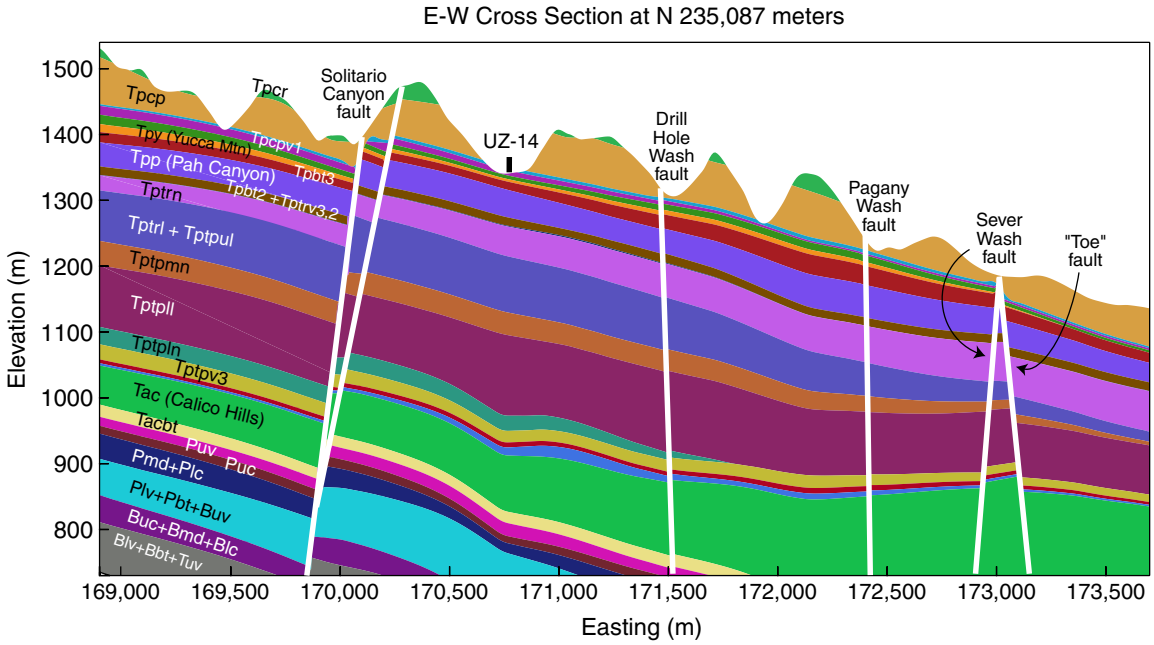


Figure 2. Hydrogeologic layers and faults in the two-dimensional vertical cross section through borehole UZ-14.

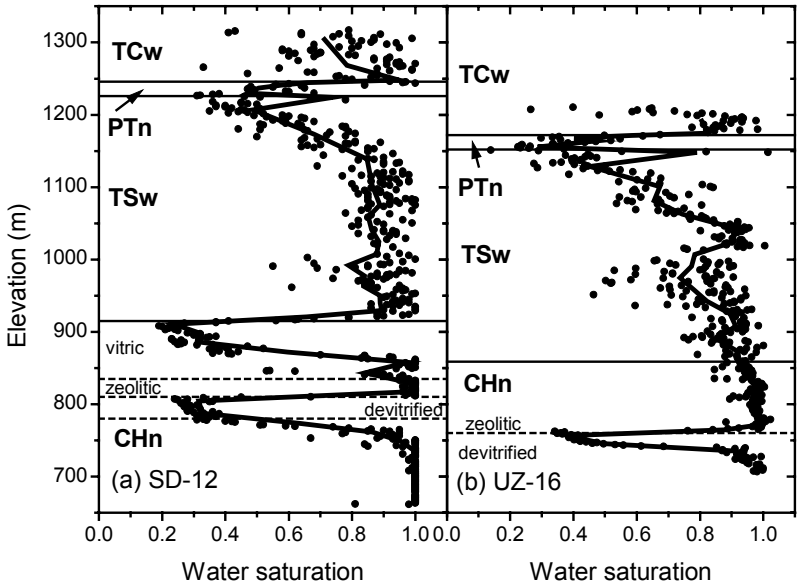


Figure 3. Vertical profiles of measured core-scale matrix water saturation (in dots) and their layer-scale values (in lines) at (a) borhole SD-12, and (b) borehole UZ-16. Observations provided by the USGS (Rousseau et al., 1997a, b; Flint, 1998a).

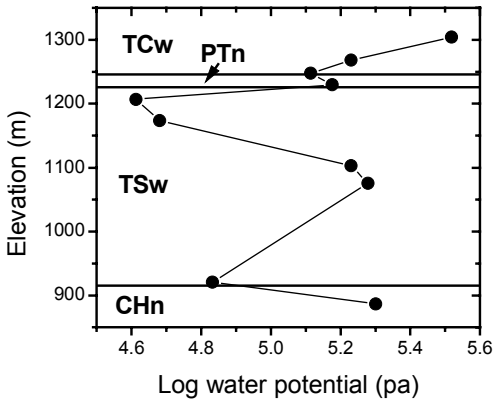


Figure 4. Vertical profile of in-situ water potential measurements at borehole SD-12. Observations provided by the USGS (Rousseau et al., 1997a).

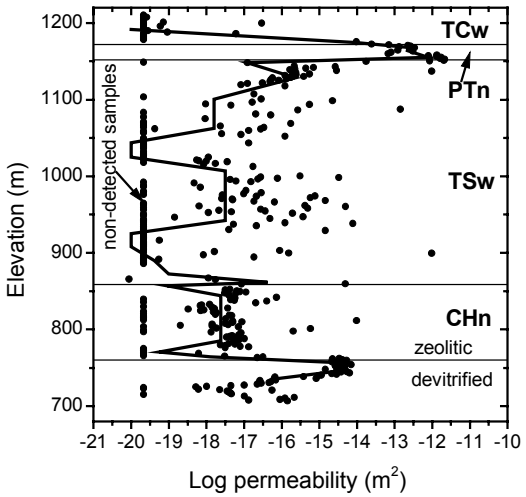


Figure 5. Vertical profile of measured core-scale matrix permeability (in dots) and the layer-scale geometric mean (in line) at the UZ-16 borehole. Observations provided by the USGS (Flint, 1998a).

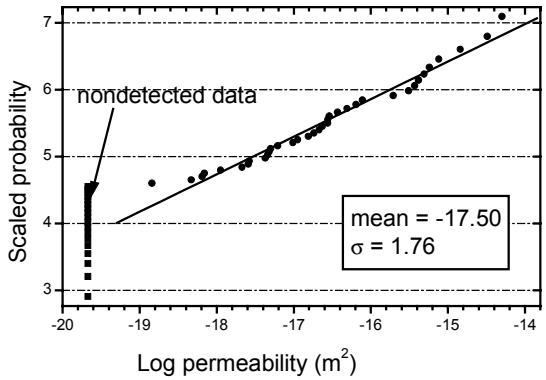


Figure 6. Estimation of the mean (the horizontal value at the scaled probability = 5) and standard deviation (the horizontal interval between two neighboring vertical ticks) of local-scale measured matrix permeability in a hydrogeologic layer at borehole UZ-16. Observations provided by the USGS (Flint, 1998a).

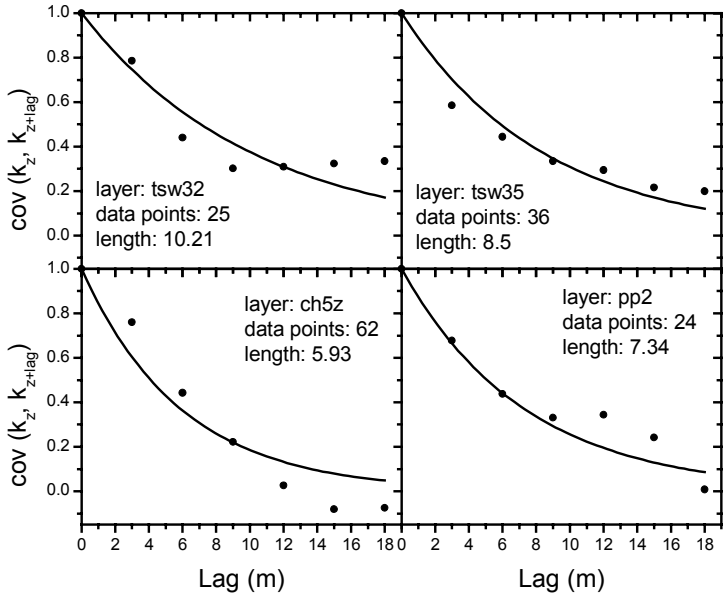


Figure 7. Estimation of vertical correlation lengths with the exponential covariance model in different layers using matrix permeability (*k*) at borehole UZ-16.

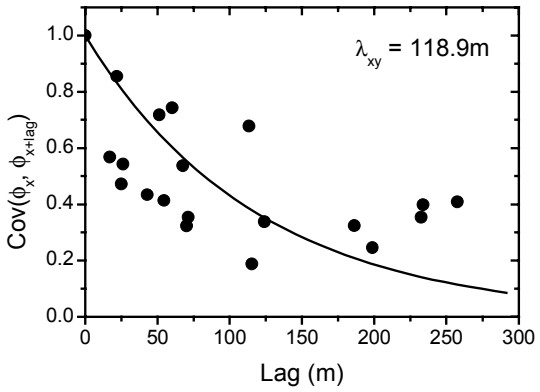


Figure 8. Estimation of average horizontal correlation length using porosity ( $\phi$ ) measurements.

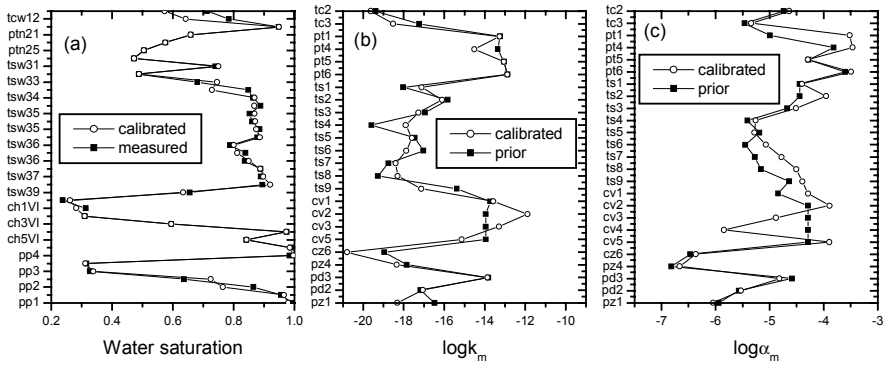


Figure 9. Match at borehole SD-12: (a) the measured water saturation profile and simulated one at the calibrated properties, (b) the prior information and the calibrated values of matrix permeability ( $k_m$ ), and (c) the prior information and calibrated values of matrix $\alpha_m$ .

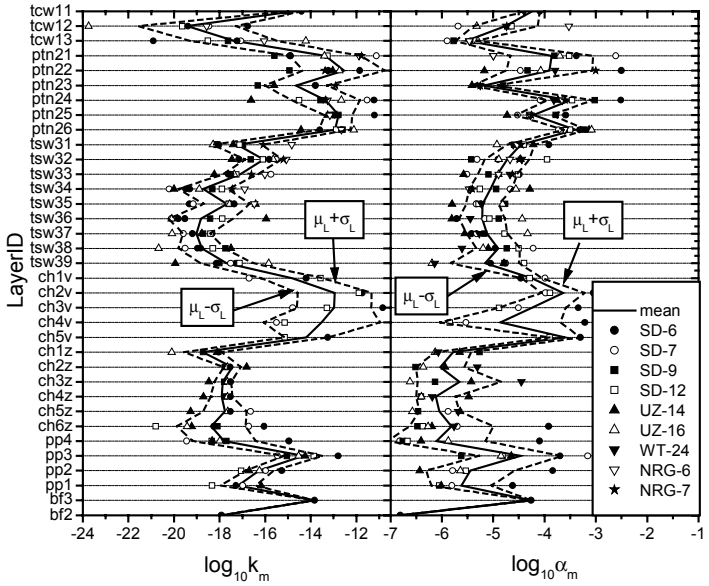


Figure 10. Spatial variability of layer-scale matrix permeability $k_m\,(m^2)$ and $\alpha_m$ (pa) obtained by individual inverse modeling using borehole measurements.

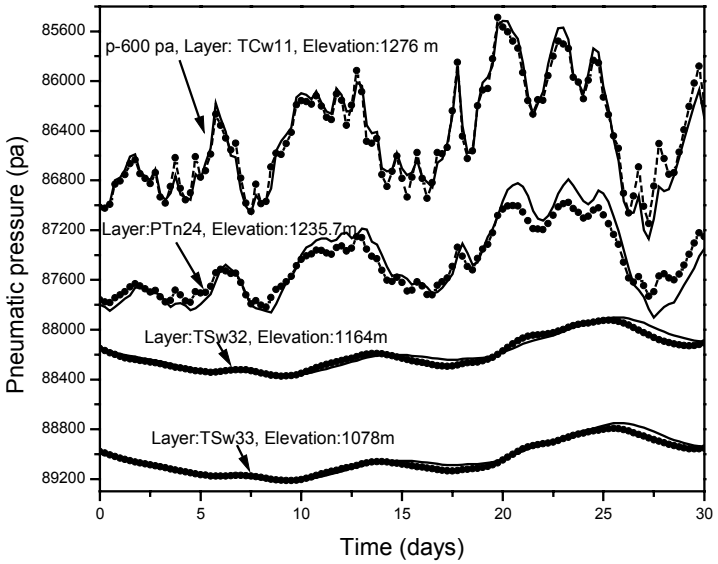


Figure 11. Match between the measured pneumatic pressure processes (in lines), and simulated ones (in line-dots) at the calibrated properties at borehole NRG-7a at four sensors at different layers and elevations. Observations from October 1994 through July 1996 provided by the USGS (Rousseau, 1996).

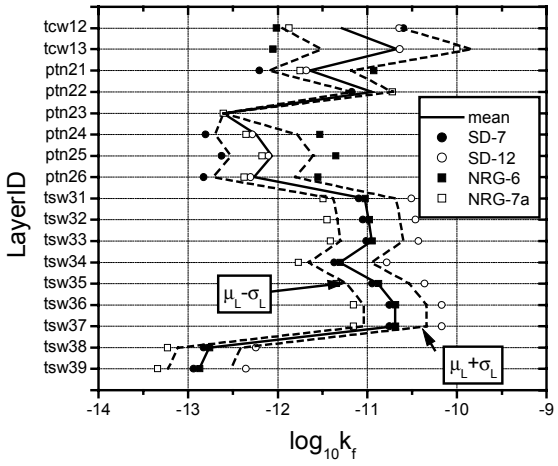


Figure 12. Spatial variability of layer-scale fracture permeability ( $m^2$ ) obtained by individual inverse modeling using borehole measurements.

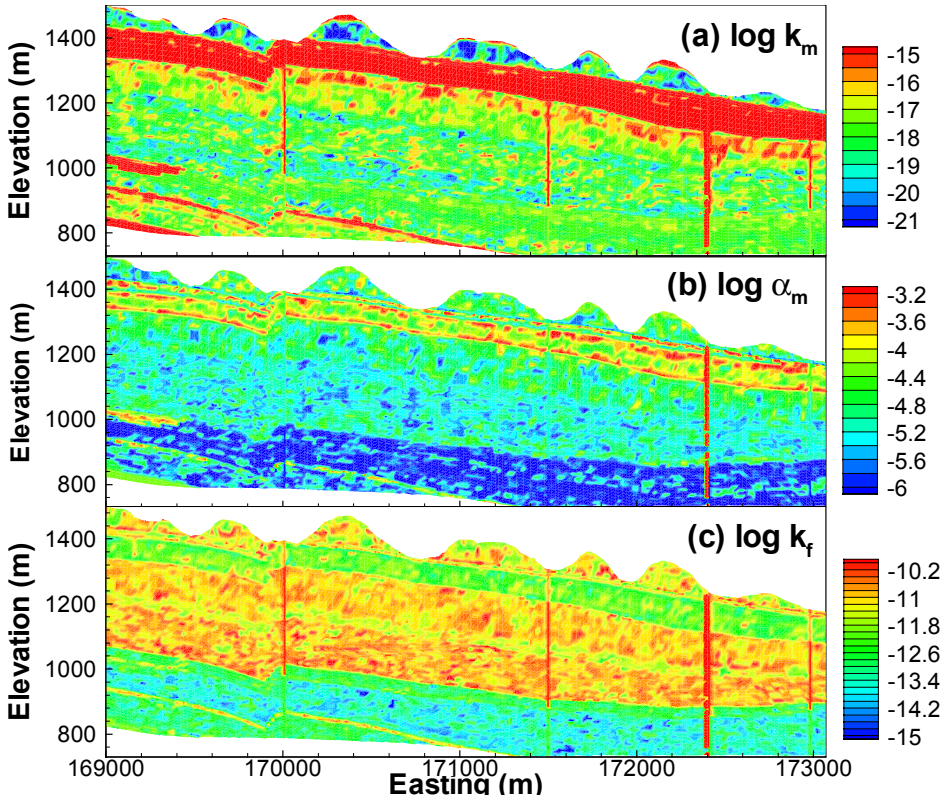


Figure 13. The random fields of matrix permeability, matrix $\alpha$, and fracture permeability in the two-dimensional vertical cross-section through borehole UZ-14 generated using multi-scale heterogeneity.

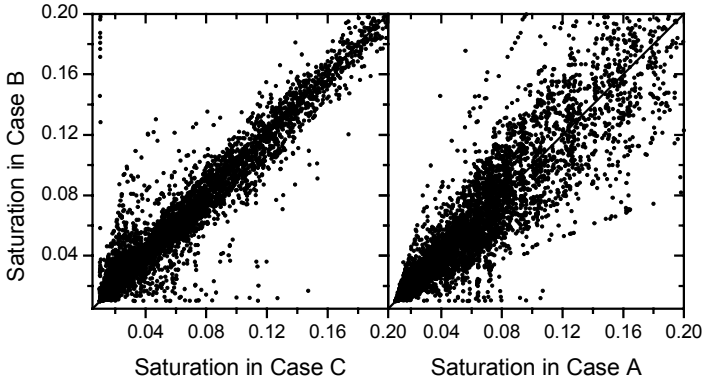


Figure 14. Comparison of simulated fracture saturation at all nodes in Cases A, B and C.

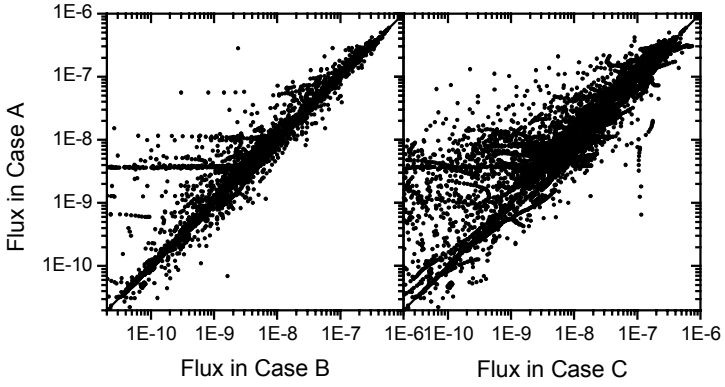


Figure 15. Comparison of simulated fracture flux (m/s) at all nodes in Cases A, B and C.

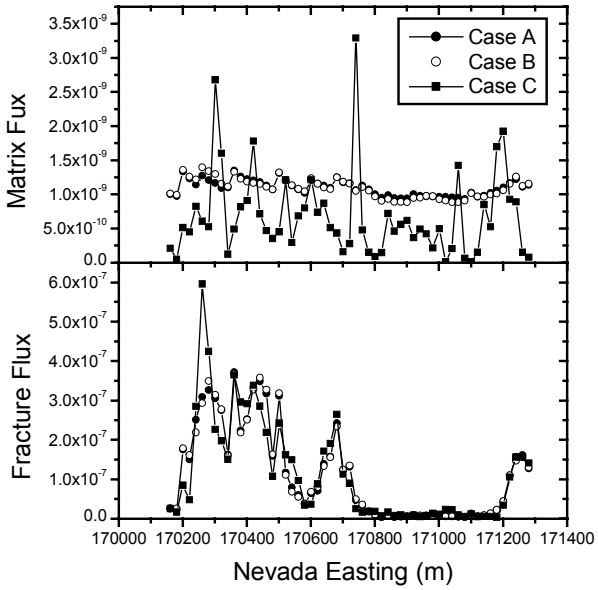


Figure 16. Comparison of simulated matrix and fracture flux (m/s) at the repository horizon in Cases A, B, and C.

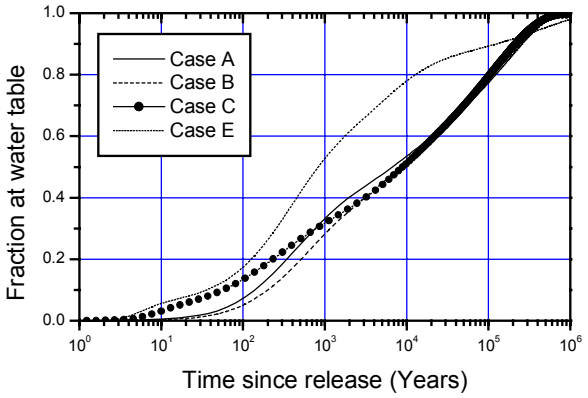


Figure 17. Comparison of breakthrough curve of the fraction of cumulative tracer mass arriving at the water table in Cases A, B, C, and E.